A Novel Microwave Tomography System Using a Rotatable Conductive Enclosure

Puyan Mojabi, *Member, IEEE*, and Joe LoVetri, *Senior Member, IEEE*

***Abstract*—A novel microwave tomography (MWT) setup is proposed wherein a rotatable conductive enclosure is used to generate electromagnetic scattering data that are collected at each static position of the enclosure using a minimal antenna array having as few as only four co-resident elements. The antenna array remains fixed with respect to the target being imaged and only the boundary of the conductive enclosure is rotated. To show that non-redundant scattering data can be generated in this way several 2D transverse magnetic imaging examples are considered using single-frequency synthetic data. For each example, the reconstruction of the complex permittivity profile is compared to that obtained using a homogeneous open-region MWT setup having 16 co-resident antennas. The weighted L_2-norm total variation multiplicative-regularized Gauss-Newton inversion (MR-GNI) is used for all inversions and for the new MWT setup the data collected at all positions of the conductive enclosure are inverted simultaneously. The quality of images obtained from the two systems is similar, but the advantage of the new configuration is its use of a fixed minimal antenna array which will put less of a burden on the numerical system model.**

***Index Terms*—Microwave tomography, inverse scattering.**

I. Introduction

CONTRIBUTIONS to microwave tomography have been made in all aspects of the technology, especially the development of improved inversion algorithms, e.g., [1]–[5]. During the past two decades, the actual physical setup used to collect the required electromagnetic scattering data has not undergone much innovation, other than the diverse antenna or transducer systems that have been reported, e.g., [6]–[13]. Obtaining good images from MWT requires the accurate collection of a substantial amount of electromagnetic scattering data, which, for efficiency, is best performed using a relatively large number of co-resident antennas. For example, in the systems described in [6] and [13] the number of elements in the arrays range from 16 to 24 where small monopoles or Vivaldi antennas have been used. The large arrays facilitate gathering bistatic scattering data at many angles without mechanically repositioning the antennas. The antenna elements themselves are typically not taken fully into account in the electromagnetic system model of the associated nonlinear optimization problem, although this is an important consideration in achieving good images (cf. the antenna compensation schemes in [14]–[16]). Including the antennas in the system model is a way of reducing the modeling error that exists between the numerical system model, used in the inversion algorithm, and the actual system, from which data is collected. Modeling error also occurs when assuming a homogeneous unbounded domain for the numerical system model (i.e., assuming that the matching fluid extends to infinity) because boundary conditions (BCs) for the dielectric discontinuity, at the MWT system's casing, are actually required to properly account for the finite extent of the matching-fluid region.

Both the antenna and the BC modeling errors can be reduced by the use of a lossy matching fluid of sufficiently high loss such that electromagnetic energy returning from the boundary or any passive antenna to any receiving antenna is not appreciable. Although this may reduce the modeling errors, the net effect of using a lossy matching fluid in MWT systems may be to reduce the accuracy of the complex permittivity profile reconstructions because the addition of any loss reduces the dynamic range and achievable signal-to-noise ratio of the system. To achieve as much accuracy and resolution as possible from an MWT system it is important to not rely on matching fluid loss to diminish both types of modeling errors (loss should only be used to reduce the contrast so as to allow more energy to penetrate the target). Thus, unless a complex numerical system model is to be used—one which accurately models the co-resident antennas as well as the boundaries of the system—the only way to reduce modeling error is to either (*i*) incorporate specialized calibration techniques for the measured data, or (*ii*) construct MWT systems that retain the capacity to provide large amounts of independent scattered field data but can be modeled accurately and efficiently.

The purpose of this paper is to propose a novel MWT system within a rotatable conductive enclosure that uses a minimal antenna array which is *fixed* with respect to the target being imaged. In this system, scattered-field data is obtained by taking bistatic measurements between each pair of elements of the fixed array at several different static positions of the rotatable enclosure. Note that this configuration is fundamentally different than existing MWT systems where either the antennas are moved with respect to a fixed object of interest or the object of interest is moved with respect to a fixed antenna array.

The inverse problem is formulated for the two-dimensional (2D) transverse magnetic (TM) case and the enclosure is chosen to have a triangular shape. Although it is not easily shown with numerical experiments using synthetic data, the practical implementation of this system should reduce both types of modeling error: the BCs at the conductive-enclosure boundary are easily

Manuscript received May 20, 2010; revised August 17, 2010; accepted November 10, 2010. Date of publication March 07, 2011; date of current version May 04, 2011. This work was supported by the Natural Sciences and Engineering Research Council of Canada.

The authors are with the Department of Electrical and Computer Engineering, University of Manitoba, Winnipeg, MB R3T5V6, Canada (e-mail: Joe_LoVetri@umanitoba.ca).

Color versions of one or more of the figures in this paper are available online at http://ieeexplore.ieee.org.

Digital Object Identifier 10.1109/TAP.2011.2123066

modeled and the antenna modeling error will be minimized because, as will be shown, small arrays with as few as four elements can be used.

The shape of the enclosure is chosen to be triangular because it is the polygon that allows the greatest number of fixed-angle step-rotations before producing a redundant configuration. We note that recently, Wadbro and Berggren have considered MWT in a rotating metallic hexagonal-shaped container where the object of interest is illuminated by waveguides connected to each side of the metallic container [17]. The container, along with the waveguides, can then be rotated to collect more scattering data and topology optimization techniques were used to invert the data [17]. At each rotation such a system produces the identical incident field with respect to the boundary of the enclosure because the sources (i.e., the waveguides) remain fixed with respect to the boundary. In the system described here, each rotation of the boundary produces a different incident field with respect to the boundary.

The paper is organized as follows. The formulation of the mathematical problem is given in Section II. In Section III, we attempt to answer the following question: *Can MWT systems with different BCs provide non-redundant scattering information about the object of interest?* Based on the observations made in Section III, the proposed system is explained in Section IV. Finally, the results will be summarized in Section V.

II. Problem Formulation

We consider the MWT problem for the 2D TM case where time-harmonic fields are used to interrogate the object of interest (OI). Thus, a time factor of $\exp(-j\omega t)$ is implicitly assumed. Consider a bounded imaging domain $\mathcal{D} \subset \mathbb{R}^2$ containing a non-magnetic OI and a measurement domain $\mathcal{S} \subset \mathbb{R}^2$ outside of the object of interest. The OI is immersed in a known non-magnetic homogeneous matching fluid with a relative complex permittivity of ϵ_b. In this paper, we assume that $\mathcal{D}$ and $\mathcal{S}$ are located either within a perfect electric conductor (PEC) of arbitrary shape or within an open region environment. In any case, the boundary condition of the environment is assumed to be known.

The complex electric contrast function is defined as

$$\chi(\boldsymbol{q}) \triangleq \frac{\epsilon_r(\boldsymbol{q}) - \epsilon_b}{\epsilon_b} \tag{1}$$

where $\boldsymbol{q}$ denotes a position vector in $\mathcal{D}$ and $\epsilon_r(\boldsymbol{q})$ is the unknown relative complex permittivity of the OI at $\boldsymbol{q}$. In MWT, the OI is successively interrogated with a number of known incident fields E_t^{inc}, where $t = 1, \ldots, T_x$ denotes the number of the active transmitter. Interaction of the incident field E_t^{inc} with the OI results in the total field E_t. The total and incident electric fields are then measured by some receiver antennas located on $\mathcal{S}$. Thus, the scattered electric field, $E_{\text{meas},t}^{\text{scat}} \triangleq E_t - E_t^{\text{inc}}$, is known at the receiver positions on $\mathcal{S}$. The goal is to find the electric contrast χ in a bounded imaging domain $\mathcal{D}$, which contains the OI, from the measured scattered fields $E_{\text{meas},t}^{\text{scat}}$ on $\mathcal{S}$. The MWT problem may then be formulated as the minimization over χ of the least-squares (LS) data misfit cost-functional

$$\mathcal{C}^{\text{LS}}(\chi) = \eta_{\mathcal{S}} \sum_{t=1}^{T_x} \left\| E_t^{\text{scat}}(\chi) - E_{\text{meas},t}^{\text{scat}} \right\|_{\mathcal{S}}^2 \tag{2}$$

where $E_t^{\text{scat}}(\chi)$ is the simulated scattered field at the observation points corresponding to the predicted contrast χ for the tth transmitter, and $\|\cdot\|_{\mathcal{S}}$ denotes the L_2-norm on $\mathcal{S}$. The weighting $\eta_{\mathcal{S}}$ is chosen to be

$$\eta_{\mathcal{S}} = \left(\sum_{t=1}^{T_x} \left\| E_{\text{meas},t}^{\text{scat}} \right\|_{\mathcal{S}}^2 \right)^{-1}. \tag{3}$$

To treat the ill-posedness of the problem, we form the multiplicative regularized cost-functional at the nth iteration of the algorithm as [5], [18], [19]

$$\mathcal{C}_n(\chi) = \mathcal{C}^{\text{LS}}(\chi) \mathcal{C}_n^{\text{MR}}(\chi). \tag{4}$$

Here, we consider the multiplicative regularizer $\mathcal{C}_n^{\text{MR}}$ as the weighted L_2-norm total variation of the unknown contrast, defined as [5], [18]

$$\mathcal{C}_n^{\text{MR}}(\chi) = \int_{\mathcal{D}} b_n^2(\boldsymbol{q}) \left(|\nabla \chi(\boldsymbol{q})|^2 + \alpha_n^2 \right) d\boldsymbol{q}. \tag{5}$$

The weighting $b_n(\boldsymbol{q})$ is chosen to be

$$b_n(\boldsymbol{q}) \triangleq A^{-\frac{1}{2}} \left(|\nabla \chi_n(\boldsymbol{q})|^2 + \alpha_n^2 \right)^{-\frac{1}{2}} \tag{6}$$

where χ_n denotes the reconstructed contrast at the $(n-1)$th iteration of the algorithm, ∇ denotes the spatial gradient operator with respect to the position vector $\boldsymbol{q}$, and A is the area of $\mathcal{D}$. The choice of the positive parameter α_n^2 is explained below.

Herein, we consider the discrete form of the MWT problem where the contrast function $\chi(\boldsymbol{q})$ is discretized into a complex vector $\underline{\chi}$. The measured scattered data on the discrete measurement domain $\mathcal{S}$ is denoted by the complex vector $\underline{E}_{\text{meas}}^{\text{scat}}$. The vector $\underline{E}_{\text{meas}}^{\text{scat}}$ is the stacked version of the measured scattered fields for each transmitter. Assuming that the tth transmitter is active, the simulated scattered field corresponding to the predicted contrast at the nth iteration of the GNI algorithm, $\underline{\chi}_n$, is denoted by $\underline{E}_{t,n}^{\text{scat}}$. The vector $\underline{E}_n^{\text{scat}}$ is then formed by stacking $\underline{E}_{t,n}^{\text{scat}}$. The positive parameter α_n^2 is chosen to be $\mathcal{F}^{\text{LS}}(\underline{\chi}_n)/\Delta A$ where $\mathcal{F}^{\text{LS}}$ represents the discrete form of $\mathcal{C}^{\text{LS}}$ and ΔA is the area of a single cell in the uniformly discretized domain $\mathcal{D}$.

Applying the Gauss-Newton Inversion (GNI) algorithm to the discrete form of (4), the contrast vector at the nth iteration of the inversion algorithm is then updated as $\underline{\chi}_{n+1} = \underline{\chi}_n + \nu_n \Delta \underline{\chi}_n$ where ν_n is an appropriate step length and $\Delta \underline{\chi}_n$ is the correction vector. In this work, we utilize the line search algorithm described in [18], [20]. The correction vector can be found from

$$\left(\underline{\boldsymbol{J}}_n^H \underline{\boldsymbol{J}}_n - \beta_n \underline{\boldsymbol{\mathcal{L}}}_n \right) \Delta \underline{\chi}_n = \underline{\boldsymbol{J}}_n^H \underline{d}_n + \beta_n \underline{\boldsymbol{\mathcal{L}}}_n \underline{\chi}_n \tag{7}$$

where $\underline{\boldsymbol{\mathcal{L}}}_n$ represents the discrete form of the $\nabla \cdot (b_n^2 \nabla)$ operator, $\underline{\boldsymbol{J}}_n$ is the Jacobian matrix which contains the derivatives of the simulated scattered field with respect to the contrast and evaluated at $\underline{\chi} = \underline{\chi}_n$. The discrepancy vector $\underline{d}_n$ is given as

$\underline{d}_n = \underline{E}^{\text{scat}}_{\text{meas}} - \underline{E}^{\text{scat}}_n$ and $\beta_n = \|\underline{d}_n\|^2$ [5], [18], [21]. We note that the regularization operator $\underline{\underline{\mathcal{L}}}_n$ is a weighted Laplacian operator which provides an edge-preserving regularization [22].

Throughout this paper, we use the outlined GNI algorithm, sometimes referred to as the multiplicative regularized Gauss-Newton inversion (MR-GNI) algorithm, to invert the synthetic data sets. All synthetic data sets are generated on a different grid than the ones used in the inversion algorithm. We also add 3% RMS additive white noise to the synthetic data set using the formula [23]

$$\underline{E}^{\text{scat}}_{\text{meas},t} = \underline{E}^{\text{scat,fwd}}_t + \max\left[\forall_t \, \underline{E}^{\text{scat,fwd}}_t\right] \frac{\eta}{\sqrt{2}}(\underline{\vartheta}_1 + j\underline{\vartheta}_2) \tag{8}$$

where $\underline{E}^{\text{scat,fwd}}_t$ is the scattered field on the measurement domain due to the tth transmitter obtained by the forward solver, $\underline{\vartheta}_1$ and $\underline{\vartheta}_2$ are two real vectors whose elements are uniformly distributed zero-mean random numbers between -1 and 1, and $\eta = 0.03$. The vector $\underline{E}^{\text{scat}}_{\text{meas}}$, constructed by stacking the vectors $\underline{E}^{\text{scat}}_{\text{meas},t}$, is then used to test inversion algorithms against synthetic data sets.

III. Different Boundary Conditions for MWT

As mentioned earlier, in most MWT systems currently in existence [6], [10]–[13], [24] the OI and the antennas are contained within an enclosed chamber, usually made from a dielectric material such as plexiglass. The dielectric chamber is usually filled with a lossy matching fluid, e.g., a 87:13 glycerin:water solution is used in the Dartmouth College microwave tomography system [1], [25]. Most MWT algorithms used to invert data from these systems assume that the matching fluid extends to infinity, not to the boundary of the dielectric casing. That is, they assume that the scattering data is collected in a homogeneous embedding. In other words, the BC for the problem will be the Sommerfeld radiation condition. We will refer to the scattering data collected in such systems as the open-region scattering data.

More recently, researchers have considered MWT where the OI and the antennas are enclosed by a circular metallic enclosure [26]–[32]. We have also considered microwave tomography inside conducting cylinders of arbitrary shapes [33]. The use of conducting enclosures imposes a zero boundary condition on the total field which can be easily modeled within the utilized inversion algorithm. We will refer to the scattering data collected in such systems as the PEC-enclosed-region scattering data. In this section, we show inversion results from the open-region and PEC-enclosed-region scattering data. For the PEC-enclosed-region scattering data, we consider PEC enclosures of two different shapes.

Calculation of the Jacobian matrix and the simulated scattered field require repeated forward solver calls. For the open-region case, we utilize the method of moments (MoM) with the conjugate gradient algorithm accelerated by the fast Fourier transform (CG-FFT). The CG-FFT forward solver is also accelerated by employing the marching-on-in-source-position technique [34]. Motivated by the desire to model arbitrary PEC boundaries with both straight and curved edges, we use a finite element method (FEM) based on triangular elements for the PEC-enclosed systems. The FEM provides an accurate and fast forward solver, and in fact, is easier to implement with a PEC boundary than with absorbing boundary conditions, which are required for a homogeneous embedding. As the FEM mesh is based on triangles, and the inverse solver based on rectangular pulse-basis functions, we interpolate as required between the two meshes with a bi-linear interpolation algorithm [33].

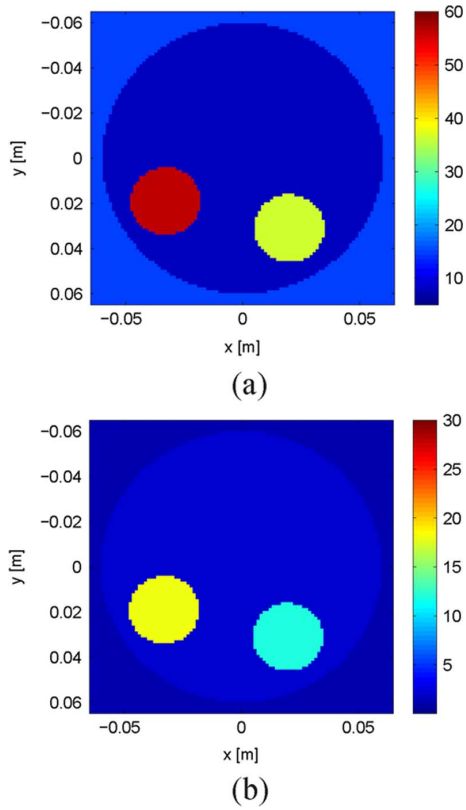

Fig. 1. Relative complex permittivity of the synthetic target I: (a) $\text{Re}(\epsilon_r)$ and (b) $\text{Im}(\epsilon_r)$.

As the first case, we consider the target shown in Fig. 1. The target consists of three circular regions. Two of these circular regions have the same radius of 0.015 m and their relative complex permittivities are $\epsilon_{r,\text{tum}} = 56.4 + j18.05$ and $\epsilon_{r,\text{fibro}} = 36.47 + j11.73$ at the frequency of 1 GHz. These two circular regions are surrounded by another circular region with radius of 0.06 m and relative permittivity of $\epsilon_{r,\text{adip}} = 7.85 + j1.9$. The relative complex permittivities $\epsilon_{r,\text{tum}}$, $\epsilon_{r,\text{fibro}}$, and $\epsilon_{r,\text{adip}}$ represent the relative complex permittivity of human breast tumor, fibroglandular, and adipose tissue respectively based on the single-pole Debye model [35]. The target is immersed in a background medium of relative complex permittivity of $15 + j$. We take three different configurations for collecting the scattering data; namely, open-region, equilateral triangular PEC-enclosed-region, and square PEC-enclosed-region. In all cases, the transmitters and receivers are evenly spaced on a circle of radius 0.1 m and the frequency of operation is 1 GHz. These configurations are shown in Fig. 2.

Two different scenarios are used to collect the scattering data. In the first scenario, 7 transmitters and 7 receivers are used for collecting the scattering data on the measurement circle. The

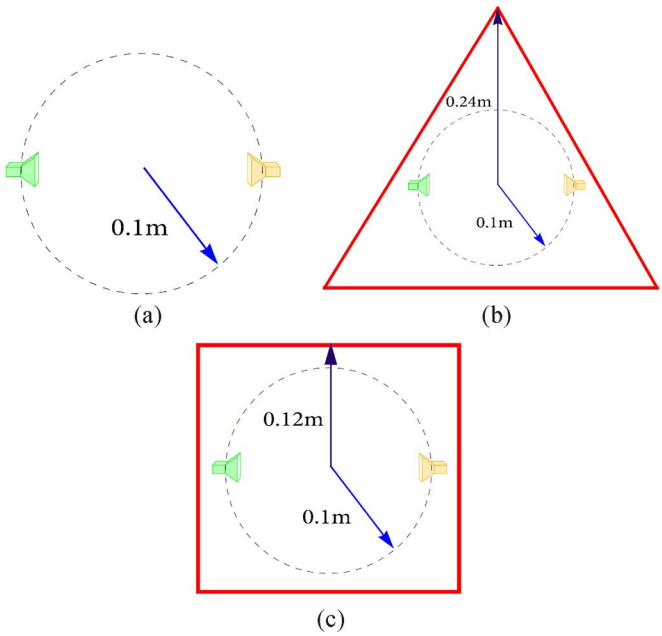

Fig. 2. (a) configuration for the open-region case, (b) configuration for the equilateral triangular PEC-enclosed-region case (the equilateral triangle is the PEC enclosure), and (c) configuration for the square PEC-enclosed-region case (the square is the PEC enclosure). The dotted circle, which has the radius of 0.1 m, shows the transmitter/receiver location (measurement domain $\mathcal{S}$).

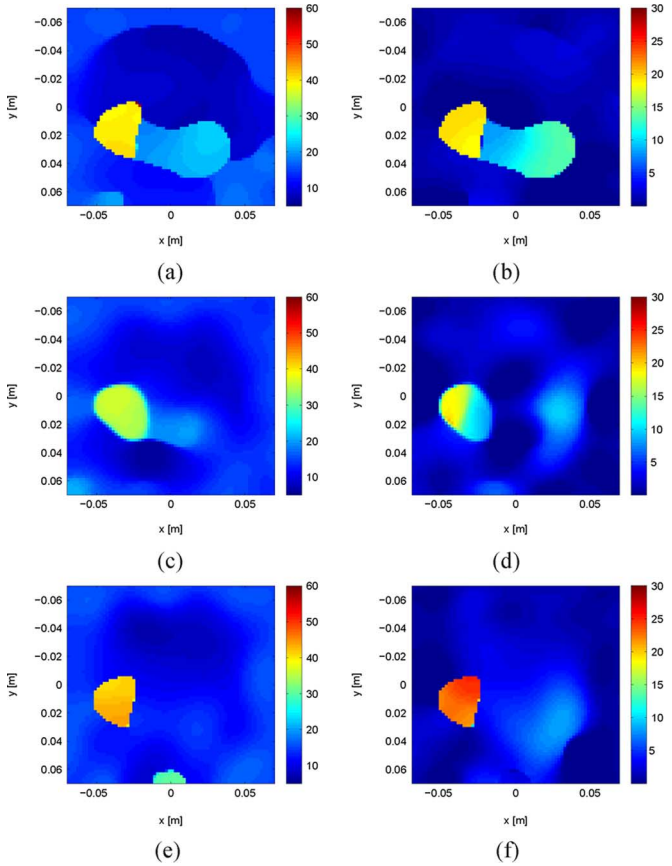

Fig. 3. 1st scenario: 7 transmitters and 7 receivers (left: $\mathrm{Re}(\epsilon_r)$ and right: $\mathrm{Im}(\epsilon_r)$) (a)–(b) inversion of the scattering data collected in the open-region embedding, (c)–(d) inversion of the scattering data collected inside the equilateral triangular PEC-enclosed embedding, and (e)–(f) inversion of the scattering data collected in the square PEC-enclosed embedding.

inversion results for these three cases are shown in Fig. 3. As can be seen, all three inversions result in poor reconstructions.

We now attempt to answer the following question: *do scattering data sets collected under different BCs provide non-redundant information about the OI?* To answer this question, we have developed an inversion algorithm to simultaneously invert the scattering data collected in different configurations. For example, for the case where there are two sets of scattering data, one collected in an open-region configuration and the other one in a PEC-enclosed-region configuration, we construct the following regularized cost-functional

$$\mathcal{C}_n(\chi) = \frac{1}{2}\left[\mathcal{C}^{\mathrm{LS}}_{\mathrm{open}}(\chi) + \mathcal{C}^{\mathrm{LS}}_{\mathrm{pec}}(\chi)\right]\mathcal{C}^{\mathrm{MR}}_n(\chi). \tag{9}$$

The cost-functionals $\mathcal{C}^{\mathrm{LS}}_{\mathrm{open}}$ and $\mathcal{C}^{\mathrm{LS}}_{\mathrm{pec}}$ represent the data misfit cost-functional, see (2), for the open-region and PEC-enclosed-region cases, respectively. The regularizer $\mathcal{C}^{\mathrm{MR}}_n$ is given in (5) and the steering parameter α_n^2, in the discrete domain, is given as

$$\alpha_n^2 = \frac{1}{2}\frac{\mathcal{F}^{\mathrm{LS}}_{\mathrm{open}}(\underline{\chi}_n) + \mathcal{F}^{\mathrm{LS}}_{\mathrm{pec}}(\underline{\chi}_n)}{\Delta A}. \tag{10}$$

where $\mathcal{F}^{\mathrm{LS}}_{\mathrm{open}}(\underline{\chi}_n)$ and $\mathcal{F}^{\mathrm{LS}}_{\mathrm{pec}}(\underline{\chi}_n)$ are the discrete forms of $\mathcal{C}^{\mathrm{LS}}_{\mathrm{open}}(\chi_n)$ and $\mathcal{C}^{\mathrm{LS}}_{\mathrm{pec}}(\chi_n)$. The correction $\Delta\underline{\chi}_n$ is then found by solving

$$\left(\underline{\underline{\boldsymbol{A}}}_n^H\underline{\underline{\boldsymbol{A}}}_n - \beta_n\underline{\underline{\boldsymbol{\mathcal{L}}}}_n\right)\Delta\underline{\chi}_n = \underline{\underline{\boldsymbol{A}}}_n^H\underline{d}_n^{\mathrm{open,pec}} + \beta_n\underline{\underline{\boldsymbol{\mathcal{L}}}}_n\underline{\chi}_n. \tag{11}$$

The complex matrix $\underline{\underline{\boldsymbol{A}}}_n$ is constructed as

$$\underline{\underline{\boldsymbol{A}}}_n = \begin{pmatrix} \sqrt{\eta_{\mathcal{S},\mathrm{open}}}\underline{\underline{\boldsymbol{J}}}_{\mathrm{open},n} \\ \sqrt{\eta_{\mathcal{S},\mathrm{pec}}}\underline{\underline{\boldsymbol{J}}}_{\mathrm{pec},n} \end{pmatrix} \tag{12}$$

where $\underline{\underline{\boldsymbol{J}}}_{\mathrm{open},n}$ and $\underline{\underline{\boldsymbol{J}}}_{\mathrm{pec},n}$ are the Jacobian matrices for the open-region and PEC-enclosed-region cases at the nth iteration of the inversion algorithm respectively. The normalization factors for the open-region and PEC-enclosed-region scattering data, $\eta_{\mathcal{S},\mathrm{open}}$ and $\eta_{\mathcal{S},\mathrm{pec}}$, are also given by (3). The vector $\underline{d}_n^{\mathrm{open,pec}}$ is given as

$$\underline{d}_n^{\mathrm{open,pec}} = \begin{pmatrix} \underline{d}_{\mathrm{open},n} \\ \underline{d}_{\mathrm{pec},n} \end{pmatrix} = \begin{pmatrix} \underline{E}^{\mathrm{scat}}_{\mathrm{open},n} - \underline{E}^{\mathrm{scat}}_{\mathrm{meas,open}} \\ \underline{E}^{\mathrm{scat}}_{\mathrm{pec},n} - \underline{E}^{\mathrm{scat}}_{\mathrm{meas,pec}} \end{pmatrix} \tag{13}$$

where $\underline{E}^{\mathrm{scat}}_{\mathrm{open},n}$ and $\underline{E}^{\mathrm{scat}}_{\mathrm{pec},n}$ are the complex vectors containing the simulated scattered field at the observation points corresponding to the predicted contrast $\underline{\chi}_n$ for the open-region and PEC-enclosed-region cases. The complex vectors $\underline{E}^{\mathrm{scat}}_{\mathrm{meas,open}}$ and $\underline{E}^{\mathrm{scat}}_{\mathrm{meas,pec}}$ represent the measured data for the open-region and PEC-enclosed-region cases. The discrete regularization operator $\underline{\underline{\boldsymbol{\mathcal{L}}}}_n$ has been described in Section II and the weight of this regularization, i.e., β_n, is

$$\beta_n = \mathcal{F}^{\mathrm{LS}}_{\mathrm{open}}(\underline{\chi}_n) + \mathcal{F}^{\mathrm{LS}}_{\mathrm{pec}}(\underline{\chi}_n). \tag{14}$$

Using this inversion algorithm, we simultaneously invert the three data sets described above (where only 7 transmitters and 7 receivers are used). In Fig. 4, we show the simultaneous inversion of (*i*) open-region and triangular PEC-enclosed-region

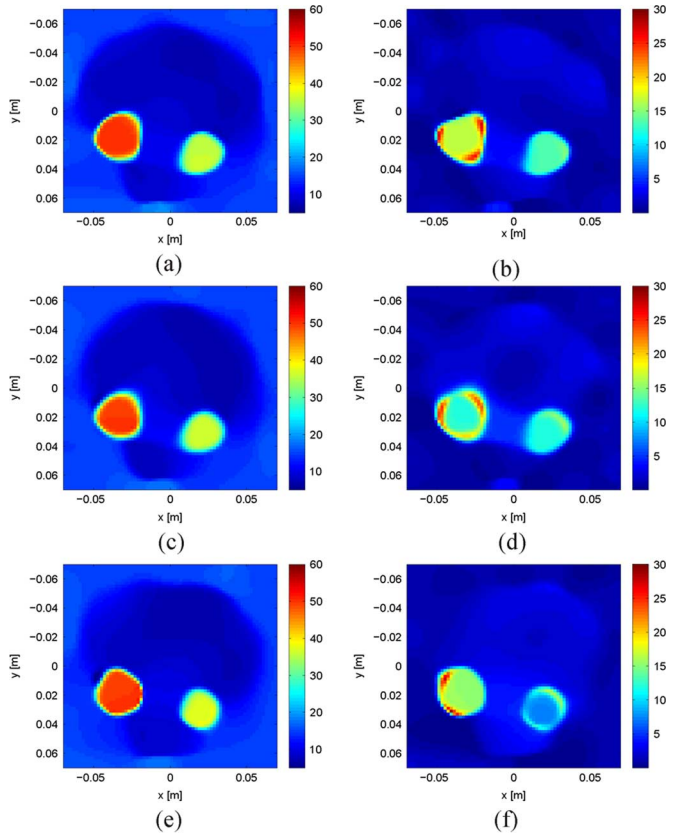

Fig. 4. 1st scenario: 7 transmitters and 7 receivers (left: $\mathrm{Re}(\epsilon_r)$ and right: $\mathrm{Im}(\epsilon_r)$); simultaneous inversion of (a)–(b) scattering data collected in the open-region and triangular PEC-enclosed region configurations, (c)–(d) scattering data collected in the open-region and square PEC-enclosed region configurations, and (e)–(f) scattering data collected in the square PEC-enclosed region and triangular PEC-enclosed region configurations.

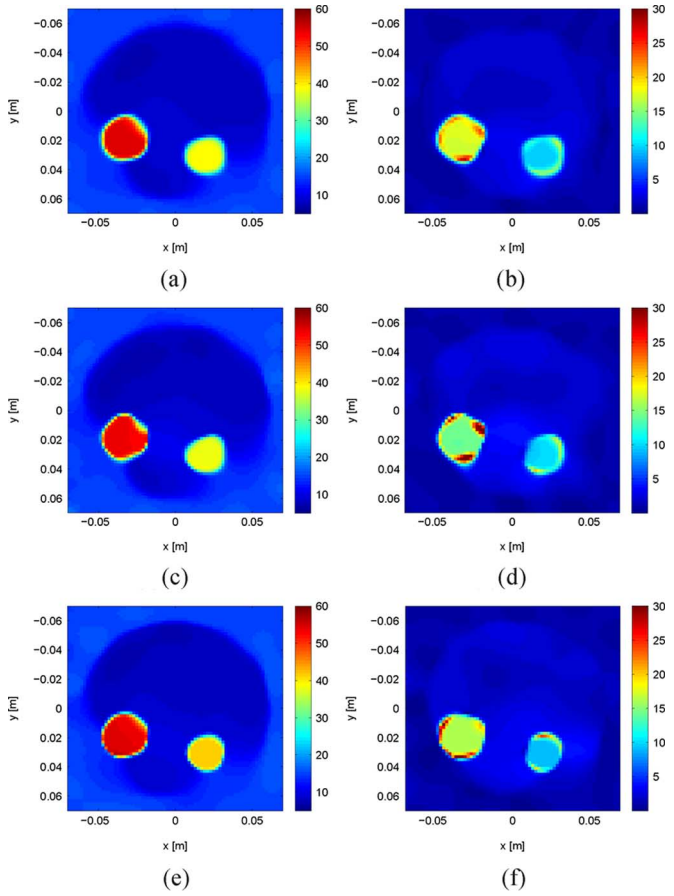

Fig. 5. 2nd scenario: 16 transmitters and 16 receivers (left: $\mathrm{Re}(\epsilon_r)$ and right: $\mathrm{Im}(\epsilon_r)$) (a)–(b) inversion of the scattering data collected in the open-region embedding, (c)–(d) inversion of the scattering data collected in the triangular PEC-enclosed embedding, and (e)–(f) inversion of the scattering data collected in the square PEC-enclosed embedding.

scattering data, (*ii*) open-region and square PEC-enclosed-region scattering data, and (*iii*) square PEC-enclosed-region and triangular PEC-enclosed-region scattering data. As can be seen, the simultaneous inversion results are very close to the true profile. Comparing Figs. 4 and 3, it can be easily seen that the simultaneous inversion has resulted in a more accurate reconstruction compared to the separate inversions of each data set. That being said, and noting that these data sets are distinguished by their corresponding BCs, it can be concluded that these three BCs have provided non-redundant information about the OI.

We now consider the second scenario for collecting the scattering data in these three configurations, where we increase the number of transmitters and receivers to 16; thus, having 256 measurements. The inversion of each data set is shown in Fig. 5. The simultaneous inversion of these data sets are shown in Fig. 6. In this scenario, the separate inversion of each data set and the simultaneous inversions result in similar reconstruction.

From these two scenarios and other similar inversion results (not shown here), it can be concluded that different BCs, at least when utilizing very few transmitters and receivers, provide non-redundant information for the reconstruction. We note that the necessary condition to obtain non-redundant information is to use a lossless or low-loss background medium so as to not suppress the reflection from the PEC enclosure. For example, if a lossy background medium with the relative complex permittivity of $23.4 + j20.3$ at 1 GHz (as the one used in the Dartmouth College MWT system [1]) is utilized, the reflection from the PEC enclosure is suppressed significantly; thus, the simultaneous inversion of open-region and PEC-enclosed-region data cannot provide a good reconstruction for the target shown in Fig. 1. In addition, from our numerical trials, we have found that if the OI has high loss, it can also suppress the reflection from the PEC enclosure; thus, reducing the amount of non-redundant information significantly.

IV. MWT System Using A Rotatable Conductive Enclosure

Based on the idea that collecting scattering data using few transceivers and under different BCs yields different usable information, we now consider a rotatable equilateral triangular metallic casing, Γ, which encloses the OI and a few transceivers, see Fig. 7. The OI is located in the bounded imaging domain $\mathcal{D} \subset \mathbb{R}^2$. The transceivers are located on the measurement domain $\mathcal{S} \subset \mathbb{R}^2$, which is outside the OI. We assume that the metallic casing is a PEC and is filled with a lossless or low-loss matching fluid with a known relative complex permittivity of ϵ_b. To obtain more scattering data by changing the BCs of the MWT system, the enclosure Γ is rotated at angles $\theta_l \in [0^\circ, 120^\circ)$, $l = 1, \ldots, L$, with respect to the fixed $\mathcal{D}$ and fixed $\mathcal{S}$ as depicted

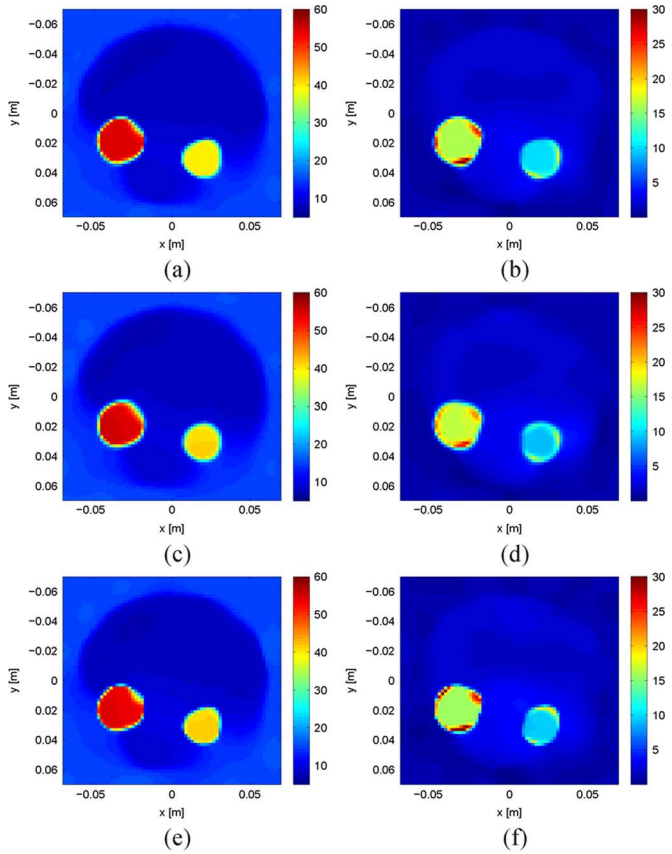

Fig. 6. 2nd scenario: 16 transmitters and 16 receivers (left: $\mathrm{Re}(\epsilon_r)$ and right: $\mathrm{Im}(\epsilon_r)$); simultaneous inversion of (a)–(b) scattering data collected in the open-region and triangular PEC-enclosed region configuration, (c)–(d) scattering data collected in the open-region and square PEC-enclosed region configurations, and (e)–(f) scattering data collected in the square PEC-enclosed and triangular PEC-enclosed region configurations.

in Fig. 7. At the lth configuration of the enclosure Γ, the OI is successively illuminated by some incident electric field, $\boldsymbol{E}^{\mathrm{inc}}_{l,t}$ where t denotes the transmitter index $(t = 1, \ldots, T_x)$. Interaction of the incident field with the OI results in the total field $\boldsymbol{E}_{l,t}$. Note that the resulting field depends not only on the transmitter location, but also on the orientation of the enclosure. The total and incident electric fields are then measured by the receiver antennas located on $\mathcal{S}$. Thus, the scattered field at the observation points, contaminated by measurement noise, is known and denoted by $\boldsymbol{E}^{\mathrm{scat}}_{\mathrm{meas},l,t}$.

The inversion problem for this system may then be formulated as the minimization over χ of the following nonlinear least-squares data misfit cost-functional

$$\mathcal{C}^{\mathrm{ROT}}(\chi) = \frac{1}{L}\sum_{l=1}^{L}\mathcal{C}^{\mathrm{LS}}_{l}(\chi) = \frac{1}{L}\sum_{l=1}^{L}\eta_{\mathcal{S},l}\sum_{t=1}^{T_x}\left\|E^{\mathrm{scat}}_{l,t}(\chi) - E^{\mathrm{scat}}_{\mathrm{meas},l,t}\right\|^2_{\mathcal{S}} \quad (15)$$

where $E^{\mathrm{scat}}_{l,t}(\chi)$ is the simulated scattered field on $\mathcal{S}$ due to a predicted contrast χ when the tth transmitter is active at the lth configuration of the triangular enclosure. The normalization factor $\eta_{\mathcal{S},l}$ is given by (3) where $E^{\mathrm{scat}}_{\mathrm{meas},t}$ needs to be replaced with $E^{\mathrm{scat}}_{\mathrm{meas},l,t}$.

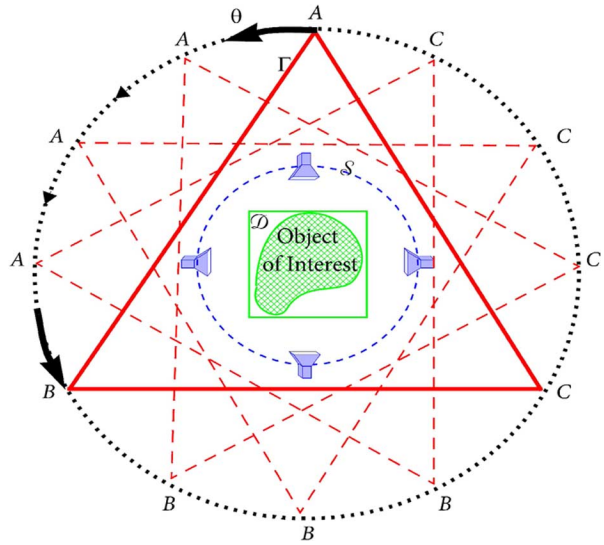

Fig. 7. The geometrical configuration of the MWT problem with a rotatable conductive triangular enclosure. The equilateral triangle, $\triangle ABC$, represents the metallic casing, which encloses the imaging domain $\mathcal{D}$ and the measurement domain $\mathcal{S}$. The dotted black circle is the circumscribing circle of the triangle. The triangular enclosure can rotate on within a circumscribing circle for θ degrees where $\theta \in [0°, 120°)$.

We regularize (15) by the weighted L_2-norm total variation multiplicative regularizer given in (5). Thus, at the nth iteration of the inversion algorithm, we minimize the regularized cost-functional

$$\mathcal{C}_n(\chi) = \mathcal{C}^{\mathrm{ROT}}(\chi)\mathcal{C}^{\mathrm{MR}}_n(\chi). \quad (16)$$

The positive parameter α^2_n in (5) is chosen to be $\mathcal{F}^{\mathrm{ROT}}(\underline{\chi}_n)/\Delta A$ where $\mathcal{F}^{\mathrm{ROT}}(\underline{\chi}_n)$ is the discrete form of $\mathcal{C}^{\mathrm{ROT}}(\chi_n)$. The correction vector $\underline{\Delta\chi}_n$ is found by solving

$$\left[\left(\sum_{l=1}^{L}\eta_{\mathcal{S},l}\underline{\boldsymbol{J}}^H_{l,n}\underline{\boldsymbol{J}}_{l,n}\right) - \beta_n\underline{\boldsymbol{\mathcal{L}}}_n\right]\Delta\underline{\chi}_n = \left(\sum_{l=1}^{L}\eta_{\mathcal{S},l}\underline{\boldsymbol{J}}^H_{l,n}\underline{d}_{l,n}\right) + \beta_n\underline{\boldsymbol{\mathcal{L}}}_n\underline{\chi}_n \quad (17)$$

The matrix $\underline{\boldsymbol{J}}_{l,n}$ is the Jacobian matrix corresponding to the lth rotation of the enclosure and at the nth iteration of the inversion algorithm, which is calculated using an FEM forward solver. The weight β_n is equal to $L \times \mathcal{F}^{\mathrm{ROT}}(\underline{\chi}_n)$. The discrepancy vector $\underline{d}_{l,n}$ is

$$\underline{d}_{l,n} = \underline{E}^{\mathrm{scat}}_{\mathrm{meas},l} - \underline{E}^{\mathrm{scat}}_{l,n}. \quad (18)$$

Inversion results are shown for two synthetic data sets that have been created with a frequency-domain FEM forward solver. In both cases, we use the equilateral triangular PEC enclosure shown in Fig. 7 and assume that the radius of the circumscribing circle of the triangle is 0.24 m. The radius of the measurement circle $\mathcal{S}$ is chosen to be 0.1 m for both data sets.

The first synthetic data set is collected from the target described in Section III and shown in Fig. 1. Similar to the inversion results shown in Section III, the frequency of operation is chosen to be 1 GHz. We consider only 4 transmitters and 4 receivers per transmitter which are evenly spaced on $\mathcal{S}$.

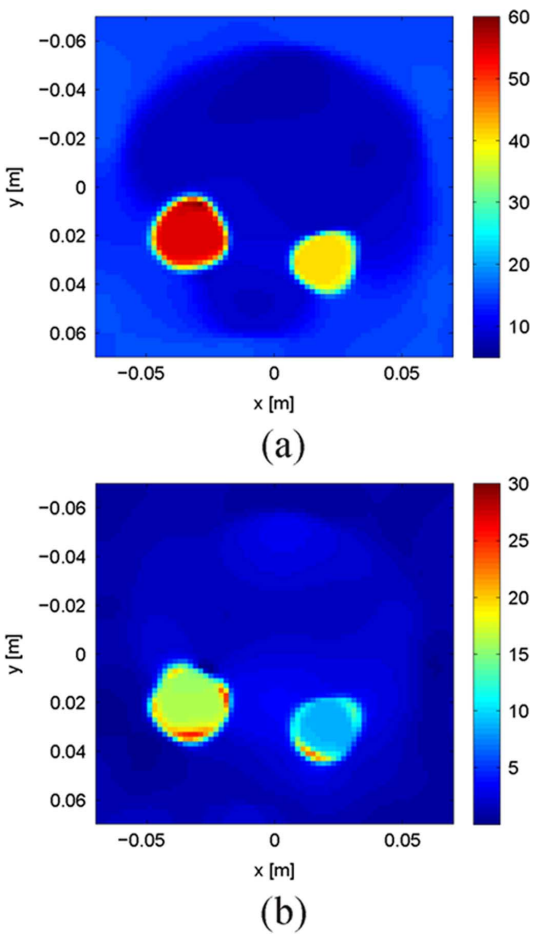

Fig. 8. Target I's reconstructed relative complex permittivity when the scattering data is collected inside the rotatable triangular conductive enclosure using 4 transmitters and 4 receivers and 12 rotations of the enclosure. (a) $\mathrm{Re}(\epsilon_r)$, (b) $\mathrm{Im}(\epsilon_r)$.

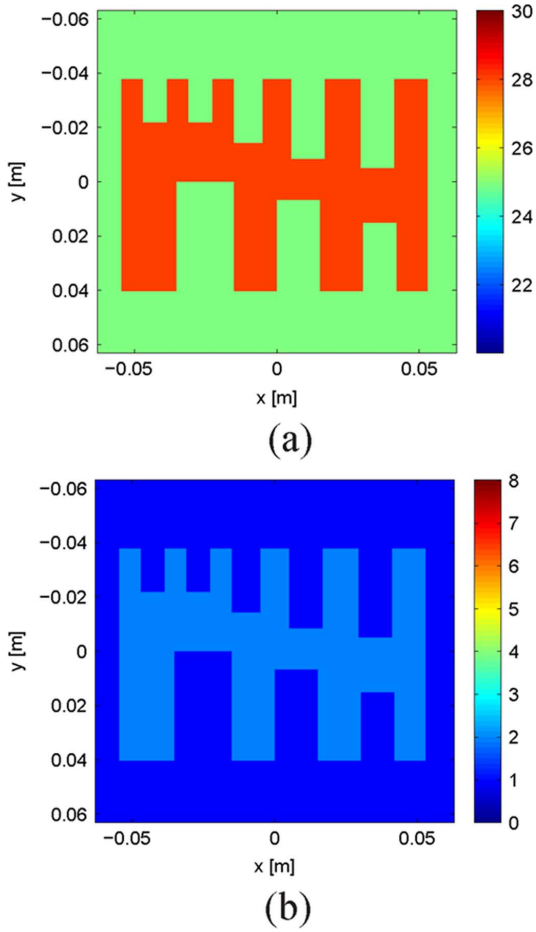

Fig. 9. Synthetic target II: true relative complex permittivity profile of the target. (a) $\mathrm{Re}(\epsilon_r)$, (b) $\mathrm{Im}(\epsilon_r)$.

Therefore, for the lth rotation of the PEC enclosure, we have $\underline{E}^{\mathrm{scat}}_{\mathrm{meas},l} \in \mathbb{C}^{16}$. The PEC enclosure is rotated 12 times ($L = 12$) with a step of 15°. Therefore, the number of measured data will be $12 \times 16 = 192$. The inversion of this scattering data, which is collected in the rotatable PEC enclosure, is shown in Fig. 8. The inversion of the scattering data collected from the same target in the open-region configuration using 16 transmitters and 16 receivers ($\underline{E}^{\mathrm{scat}}_{\mathrm{meas}} \in \mathbb{C}^{256}$) is shown in Fig. 5(a) and (b). As can be seen, the reconstruction inside the rotating PEC enclosure with only 4 transceivers and the reconstruction inside the open-region configurations with 16 transceivers are very similar for this target and both provide a reasonable reconstruction for both the real and imaginary parts of the target's relative complex permittivity.

Finally, we consider the target shown in Fig. 9. This target has the same geometry as the target used in [36] and [37] for a resolution test study. This target has different distances between its details ranging from 8 mm to 20 mm. The relative complex permittivity of the target is $28 + j2$ and that of the background medium is $25 + j$ at the frequency of operation which is chosen to be 2 GHz. To collect scattered field data, we consider 6 transmitters and 6 receivers per transmitter; thus, $\underline{E}^{\mathrm{scat}}_{\mathrm{meas},l} \in \mathbb{C}^{36}$. The PEC enclosure is then rotated 48 times with a step of 2.5°; thus, providing $48 \times 36 = 1728$ scattering measurements. The inversion of the scattering data collected inside the rotating PEC enclosure is shown in Fig. 10(a) and (b), while the inversion of the scattering data collected in the open-region embedding using 16 transmitters and 16 receivers is shown in Fig. 10(c) and (d). In both cases, the real part of the permittivity is reconstructed well but the imaginary part is poorly reconstructed. This is due to the fact that the real and imaginary parts of the OI's contrast are out of balance [38] and also the imaginary part of the contrast is very small (≈ 0.03). To get a better reconstruction for this target, we apply the image enhancement method, as outlined in [39], to the final reconstructions of both inversions. The enhanced reconstructions for both cases are shown in Fig. 11. We note that this image enhancement algorithm does not use any *a priori* information about the OI and is effectively a deblurring algorithm. To have the same number of data points as the open-region configuration, we also tried to reconstruct the target shown in Fig. 9 using 4 transceivers and 16 rotations (thus, providing 256 data points), but the inversion could not resolve all the features of this target. Therefore, the number of data collected does not equal to the amount of useful information for reconstruction purpose. Investigating the amount of information available by rotating or moving BCs with fixed sources is a topic for future study.

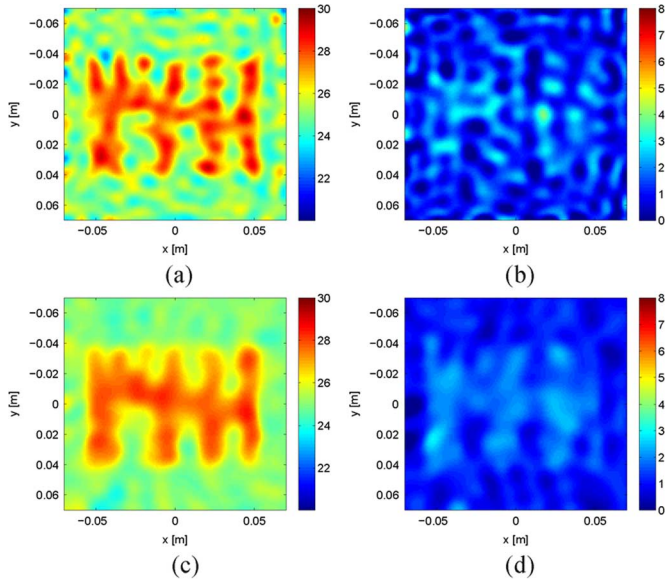

Fig. 10. Target II: (left: $\mathrm{Re}(\epsilon_r)$ and right: $\mathrm{Im}(\epsilon_r)$) (a)–(b) reconstructed relative complex permittivity when the scattering data is collected inside the rotating triangular conducting enclosure using 6 transmitters and 6 receivers and 48 rotations of the enclosure (c)–(d) reconstructed relative complex permittivity when the scattering data is collected in the open-region embedding using 16 transmitters and 16 receivers.

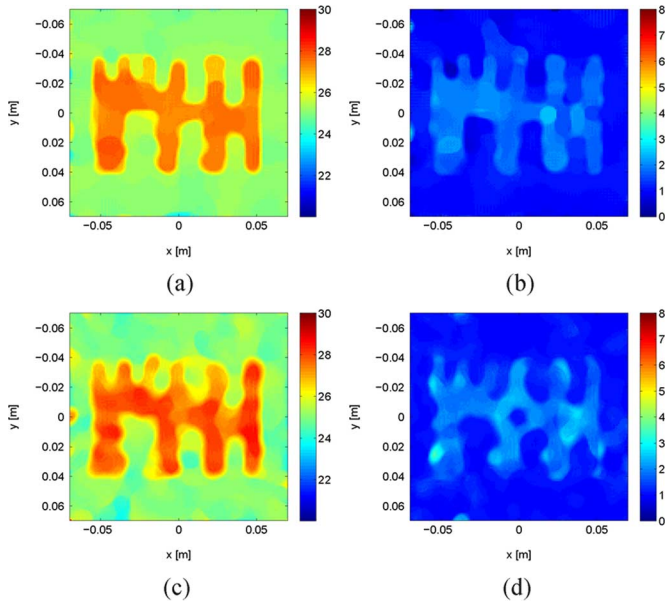

Fig. 11. Target II: (left: $\mathrm{Re}(\epsilon_r)$ and right: $\mathrm{Im}(\epsilon_r)$) reconstruction results after applying the enhancement algorithm inside (a)–(b) the rotatable triangular conductive enclosure with 6 transmitters and 6 receivers and 48 rotations, and (c)–(d) the open-region embedding with 16 transmitters and 16 receivers.

V. Conclusion

Using synthetic data sets, the possibility of imaging inside a rotatable triangular conductive enclosure using a minimal antenna array having as few as only four or six co-resident elements immersed in a low-loss background medium has been demonstrated for the 2D TM case. This study may result in the development of MWT systems which introduce less modeling error to MWT algorithms compared to the existing MWT systems while maintaining the ability to collect sufficient scattering information about the OI. Considering that the modeling error can be thought of as part of the manifest noise, and noting that the achievable resolution limit is affected by the signal-to-noise ratio [36], [40], the proposed MWT system may offer an enhanced spatial resolution over the existing MWT systems. Finally, we note that the rotatable triangular conductive enclosure is just one practical implementation of a system which uses different PEC BCs to obtain non-redundant information about an OI.

Acknowledgment

The authors thank A. Zakaria for providing the FEM solver.

References

[1] T. Rubæk, P. M. Meaney, P. Meincke, and K. D. Paulsen, "Nonlinear microwave imaging for breast-cancer screening using Gauss-Newton's method and the CGLS inversion algorithm," *IEEE Trans. Antennas Propag.*, vol. 55, no. 8, pp. 2320–2331, Aug. 2007.

[2] A. Abubakar, P. M. van den Berg, and J. J. Mallorqui, "Imaging of biomedical data using a multiplicative regularized contrast source inversion method," *IEEE Trans. Microwave Theory Tech.*, vol. 50, no. 7, pp. 1761–1777, Jul. 2002.

[3] J. D. Zaeytijd, A. Franchois, C. Eyraud, and J.-M. Geffrin, "Full-wave three-dimensional microwave imaging with a regularized Gauss-Newton method—Theory and experiment," *IEEE Trans. Antennas Propag.*, vol. 55, no. 11, pp. 3279–3292, Nov. 2007.

[4] W. C. Chew and Y. M. Wang, "Reconstruction of two-dimensional permittivity distribution using the distorted Born iterative method," *IEEE Trans. Med. Imaging*, vol. 9, no. 2, pp. 218–225, 1990.

[5] P. Mojabi and J. LoVetri, "Microwave biomedical imaging using the multiplicative regularized Gauss-Newton inversion," *IEEE Antennas and Wireless Propag. Lett.*, vol. 8, pp. 645–648, 2009.

[6] P. Meaney, M. Fanning, D. Li, S. Poplack, and K. Paulsen, "A clinical prototype for active microwave imaging of the breast," *IEEE Trans. Microwave Theory Tech.*, vol. 48, no. 11, pp. 1841–1853, Nov. 2000.

[7] A. Franchois, A. Joisel, C. Pichot, and J.-C. Bolomey, "Quantitative microwave imaging with a 2.45-GHz planar microwave camera," *IEEE Trans. Med. Imag.*, vol. 17, no. 4, pp. 550–561, Aug. 1998.

[8] A. Broquetas, J. Romeu, J. Rius, A. Elias-Fuste, A. Cardama, and L. Jofre, "Cylindrical geometry: A further step in active microwave tomography," *IEEE Trans. Microwave Theory Tech.*, vol. 39, no. 5, pp. 836–844, May 1991.

[9] S. Y. Semenov, R. H. Svenson, A. E. Bulyshev, A. E. Souvorov, A. G. Nazarov, Y. E. Sizov, V. G. Posukh, A. Pavlovsky, P. N. Repin, A. N. Starostin, B. A. Voinov, M. Taran, G. P. Tastis, and V. Y. Baranov, "Three-dimensional microwave tomography: Initial experimental imaging of animals," *IEEE Trans. Biomed. Eng.*, vol. 49, no. 1, pp. 55–63, Jan. 2002.

[10] A. Fhager, P. Hashemzadeh, and M. Persson, "Reconstruction quality and spectral content of an electromagnetic time-domain inversion algorithm," *IEEE Trans. Biomed. Eng.*, vol. 53, no. 8, pp. 1594–1604, Aug. 2006.

[11] C. Yu, M. Yuan, J. Stang, E. Bresslour, R. George, G. Ybarra, W. Joines, and Q. H. Liu, "Active microwave imaging II: 3-D system prototype and image reconstruction from experimental data," *IEEE Trans. Microwave Theory Tech.*, vol. 56, no. 4, pp. 991–1000, Apr. 2008.

[12] T. Rubaek, O. Kim, and P. Meincke, "Computational validation of a 3-D microwave imaging system for breast-cancer screening," *IEEE Trans. Antennas Propag.*, vol. 57, no. 7, pp. 2105–2115, Jul. 2009.

[13] C. Gilmore, P. Mojabi, A. Zakaria, M. Ostadrahimi, C. Kaye, S. Noghanian, L. Shafai, S. Pistorius, and J. LoVetri, "A wideband microwave tomography system with a novel frequency selection procedure," *IEEE Trans. Biomed. Eng.*, vol. 57, no. 4, pp. 894–904, Apr. 2010.

[14] K. Paulsen and P. Meaney, "Nonactive antenna compensation for fixed array microwave imaging. I. Model development," *IEEE Trans. Med. Imag.*, vol. 18, no. 6, pp. 496–507, Jun. 1999.

[15] P. Meaney, K. Paulsen, J. Chang, M. Fanning, and A. Hartov, "Nonactive antenna compensation for fixed-array microwave imaging. II. Imaging results," *IEEE Trans. Med. Imag.*, vol. 18, no. 6, pp. 508–518, Jun. 1999.

[16] O. Franza, N. Joachimowicz, and J.-C. Bolomey, "SICS: A sensor interaction compensation scheme for microwave imaging," *IEEE Trans. Antennas Propag.*, vol. 50, no. 2, pp. 211–216, Feb. 2002.

[17] E. Wadbro and M. Berggren, "Microwave tomography using topology optimization techniques," *SIAM J. Sci. Comput.*, vol. 30, no. 3, pp. 1613–1633, 2008.
[18] A. Abubakar, T. Habashy, V. Druskin, L. Knizhnerman, and D. Alumbaugh, "2.5D forward and inverse modeling for interpreting low-frequency electromagnetic measurements," *Geophysics*, vol. 73, no. 4, pp. F165–F177, Jul.–Aug. 2008.
[19] P. Mojabi and J. LoVetri, "Overview and classification of some regularization techniques for the Gauss-Newton inversion method applied to inverse scattering problems," *IEEE Trans. Antennas Propag.*, vol. 57, no. 9, pp. 2658–2665, Sept. 2009.
[20] T. M. Habashy and A. Abubakar, "A general framework for constraint minimization for the inversion of electromagnetic measurements," *Progr. Electromagn. Res.*, vol. 46, pp. 265–312, 2004.
[21] P. Mojabi, "Investigation and Development of Algorithms and Techniques for Microwave Tomography" Ph.D. dissertation, Univ. Manitoba, Winnipeg, Manitoba, Canada, 2010 [Online]. Available: URL: http://mspace.lib.umanitoba.ca/handle/1993/3946
[22] P. Charbonnier, L. Blanc-Féraud, G. Aubert, and M. Barlaud, "Deterministic edge-preserving regularization in computed imaging," *IEEE Trans. Image Processing*, vol. 6, no. 2, pp. 298–311, Feb. 1997.
[23] A. Abubakar, P. M. van den Berg, and S. Y. Semenov, "A robust iterative method for Born inversion," *IEEE Trans. Geosci. Remote Sensing*, vol. 42, no. 2, pp. 342–354, Feb. 2004.
[24] A. E. Bulyshev, A. E. Souvorov, S. Y. Semenov, R. H. Svenson, A. G. Nazarov, Y. E. Sizov, and G. P. Tastis, "Three dimensional microwave tomography. Theory and computer experiments in scalar approximation," *Inverse Probl.*, vol. 16, pp. 863–875, 2000.
[25] P. M. Meaney, M. W. Fanning, T. Raynolds, C. J. Fox, Q. Fang, C. A. Kogel, S. P. Poplack, and K. D. Paulsen, "Initial clinical experience with microwave breast imaging in women with normal mammography," *Acad Radiol.*, Mar. 2007.
[26] L. Crocco and A. Litman, "On embedded microwave imaging systems: Retrievable information and design guidelines," *Inverse Prob.*, vol. 25, no. 6, p. 17, 2009, 065001.
[27] C. Gilmore and J. LoVetri, "Enhancement of microwave tomography through the use of electrically conducting enclosures," *Inverse Prob.*, vol. 24, no. 3, p. 21, 2008, 035008.
[28] C. Gilmore and J. LoVetri, "Corrections to the 'enhancement of microwave tomography through the use of electrically conducting enclosures'," *Inverse Prob.*, vol. 26, no. 1, p. 7, Jan. 2010, 019801.
[29] A. Franchois and A. G. Tijhuis, "A quasi-Newton reconstruction algorithm for a complex microwave imaging scanner environment," *Radio Sci.*, vol. 38, no. 2, 2003.
[30] R. Lencrerot, A. Litman, H. Tortel, and J.-M. Geffrin, "Measurement strategies for a confined microwave circular scanner," *Inverse Prob. Sci. Engrg.*, pp. 1–16, Jan. 2009.
[31] R. Lencrerot, A. Litman, H. Tortel, and J.-M. Geffrin, "Imposing Zernike representation for imaging two-dimensional targets," *Inverse Prob.*, vol. 25, no. 3, p. 21, 2009, 035012.
[32] P. Mojabi and J. LoVetri, "Eigenfunction contrast source inversion for circular metallic enclosures," *Inverse Prob.*, vol. 26, no. 2, p. 23, Feb. 2010, 025010.
[33] P. Mojabi, C. Gilmore, A. Zakaria, and J. LoVetri, "Biomedical microwave inversion in conducting cylinders of arbitrary shapes," in *Proc. 13th Int. Symp. on Antenna Technology and Applied Electromagnetics and the Canadian Radio Science Meeting*, Feb. 2009, pp. 1–4.
[34] A. G. Tijhuis, K. Belkebir, and A. C. S. Litman, "Theoretical and computational aspects of 2-D inverse profiling," *IEEE Trans. Geosci. Remote Sensing*, vol. 39, no. 6, pp. 1316–1330, 2001.
[35] M. Lazebnik, M. Okoniewski, J. Booske, and S. Hagness, "Highly accurate Debye models for normal and malignant breast tissue dielectric properties at microwave frequencies," *IEEE Microw. Wireless Compon. Lett.*, vol. 17, no. 12, pp. 822–824, Dec. 2007.
[36] S. Semenov, R. Svenson, A. Bulyshev, A. Souvorov, A. Nazarov, Y. Sizov, V. Posukh, A. Pavlovsky, P. Repin, and G. Tatsis, "Spatial resolution of microwave tomography for detection of myocardial ischemia and infarction-experimental study on two-dimensional models," *IEEE Trans. Microwave Theory Tech.*, vol. 48, no. 4, pp. 538–544, Apr. 2000.
[37] C. Gilmore, P. Mojabi, A. Zakaria, S. Pistorius, and J. LoVetri, "On super-resolution with an experimental microwave tomography system," *IEEE Antennas Wireless Propag. Lett.*, vol. 9, pp. 393–396, 2010.
[38] P. Meaney, N. Yagnamurthy, and K. D. Paulsen, "Pre-scaled two-parameter Gauss-Newton image reconstruction to reduce property recovery imbalance," *Phys. Med. Biol.*, vol. 47, pp. 1101–1119, 2002.
[39] P. Mojabi and J. LoVetri, "Enhancement of the Krylov subspace regularization for microwave biomedical imaging," *IEEE Trans. Med. Imag.*, vol. 28, no. 12, pp. 2015–2019, Dec. 2009.
[40] P. Meaney, K. Paulsen, A. Hartov, and R. Crane, "Microwave imaging for tissue assessment: Initial evaluation in multitarget tissue-equivalent phantoms," *IEEE Trans. Biomed. Eng.*, vol. 43, no. 9, pp. 878–890, Sept. 1996.

Puyan Mojabi (M'10) received the B.Sc. degree in electrical and computer engineering from the University of Tehran, Tehran, Iran, in 2002, the M.Sc. degree in electrical engineering from Iran University of Science and Technology, Tehran, Iran, in 2004 and the Ph.D. degree in electrical engineering from the University of Manitoba, Winnipeg, MB, Canada, in 2010.

His current research interests are computational electromagnetics, microwave tomography and inverse problems.

Joe LoVetri (SM'00) was born in Enna, Italy, in 1963. He received the B.Sc. (with distinction) and M.Sc. degrees, both in electrical engineering, from the University of Manitoba, Winnipeg, MB, Canada, in 1984 and 1987, respectively, and the Ph.D. degree in electrical engineering from the University of Ottawa, Ottawa, ON, Canada, in 1991.

From 1984 to 1986, he was an EMI/EMC Engineer at Sperry Defence Division, Winnipeg, Manitoba. From 1986 to 1988, he held the position of TEMPEST Engineer at the Communications Security Establishment in Ottawa. From 1988 to 1991, he was a Research Officer at the Institute for Information Technology, National Research Council of Canada. From 1991 to 1999, he was an Associate Professor in the Dept. of Electrical and Computer Engineering, The University of Western Ontario. In 1997/98, he spent a sabbatical year at the TNO Physics and Electronics Laboratory, The Netherlands. Since 1999, he has been a Professor in the Department of Electrical and Computer Engineering, University of Manitoba, and was Associate Dean, Research, from 2004 to 2009. His main interests lie in time-domain computational electromagnetics, modeling of electromagnetic compatibility problems, microwave tomography and inverse problems.